

# Simulation of the Far-Infrared Polarimetry Approach Envisioned for the PRIMA Mission\*

C. DARREN DOWELL,<sup>1</sup> BRANDON S. HENSLEY,<sup>1</sup> AND MARC SAUVAGE<sup>2</sup>

<sup>1</sup>*Jet Propulsion Laboratory, California Institute of Technology, 4800 Oak Grove Drive, Pasadena, CA 91109, USA*

<sup>2</sup>*Université Paris-Saclay, Université Paris Cité, CEA, CNRS, AIM, 91191, Gif-sur-Yvette, France*

## ABSTRACT

Interest in the study of magnetic fields and the properties of interstellar dust, explored through increasingly capable far-IR/submillimeter polarimetry, along with maturing detector technology, have set the stage for a transformative leap in polarization mapping capability using a cryogenic space telescope. We describe the approach pursued by the proposed Probe far-Infrared Mission for Astrophysics (PRIMA) to make ultra-deep maps of intensity and polarization in four bands in the 91–232  $\mu\text{m}$  range. A simple, polarimetry-optimized PRIMA Polarimetric Imager (PPI) is designed for this purpose, consisting of arrays of single-polarization Kinetic Inductance Detectors oriented with three angles which allow measurement of Stokes  $I$ ,  $Q$ , and  $U$  in single scans. In this study, we develop an end-to-end observation simulator to perform a realistic test of the approach for the case of mapping a nearby galaxy. The observations take advantage of a beam-steering mirror to perform efficient, two-dimensional, crossing scans. Map making is based on ‘destriping’ approaches demonstrated for Herschel<sup>a)</sup>/SPIRE and Planck. Taking worst-case assumptions for detector sensitivity including  $1/f$  noise, we find excellent recovery of simulated input astrophysical maps, with  $I$ ,  $Q$ , and  $U$  detected at near fundamental limits. We describe how PPI performs detector relative calibration and mitigates the key systematic effects to accomplish PRIMA polarization science goals.

## 1. INTRODUCTION

The advent of sensitive observations of the polarized far-infrared (FIR) to submillimeter emission from interstellar dust over the last two decades has had broad impact across astrophysics. Dust grains preferentially align with their short axes parallel to the local magnetic field, and so the dust polarization angle is a measure of the magnetic field orientation projected onto the plane of the sky (Purcell 1975; Andersson et al. 2015). The relationship between dust, gas, and magnetic fields revealed through such observations has informed models of star formation (e.g., Planck Collaboration Int. XXXV 2016; Pattle & Fissel 2019; Pillai et al. 2020; Arzoumanian et al. 2021; Ward-Thompson et al. 2023), the structure of magnetic fields (e.g., Planck Collaboration Int. XLII 2016; Fissel et al. 2019; Borlaff et al. 2023; Surgent et al. 2023), interstellar turbulence (e.g., Soler et al. 2016; Caldwell et al. 2017; Planck Collaboration

XII 2020), interstellar filaments (e.g., Clark et al. 2015; Planck Collaboration Int. XXXIII 2016; Huffenberger et al. 2020; Ching et al. 2022; Ngoc et al. 2023), dust composition (e.g., Guillet et al. 2018; Draine & Hensley 2021; Hensley & Draine 2023; Ysard et al. 2024), and grain alignment (e.g., Hildebrand et al. 1999; Tram et al. 2021; Hoang et al. 2023; Le Gouellec et al. 2023) across environments from star-forming cores to the diffuse interstellar medium (ISM) of the Milky Way to resolved nearby galaxies, with some recent observations even at cosmological redshifts (Geach et al. 2023).

Neglecting circular polarization, which is rare in this astrophysical context, the polarization information consists of three elements to be measured at each of many points on the sky: described by either a total intensity, a polarization fraction, and a polarization angle; or alternatively the first three components of the Stokes vector ( $I, Q, U$ ) where  $I$  is the total intensity and  $Q$  and  $U$  specify the linearly-polarized intensity. A variety of strategies have emerged for mapping those three quantities for far-infrared continuum radiation, involving choices of detectors, optics, and motion of the optical boresight on the sky. Measurement of the polarization of light is inherently differential, so all methods involve subtraction

charles.d.dowell@jpl.nasa.gov

\* © 2024. All rights reserved.

<sup>a)</sup> Herschel is an ESA space observatory with science instruments provided by European-led Principal Investigator consortia and with important participation from NASA.

of detector signals, either simultaneous within common optical paths or separated in time.

There exist three broad families of detectors: (1) Dual-polarization detectors. These use two co-located elements sensing orthogonal linear polarizations, e.g., Planck (Lamarre et al. 2010), POLARBEAR (Barron et al. 2014), or the SPICA/B-BOP design (Adami et al. 2019). Dual-polarization detectors directly measure  $I$  and one polarization Stokes parameter, and they mitigate certain systematic effects such as common-mode drifts and pointing error. (2) Single-polarization detectors. Though they are simpler to design, there are relatively few instruments employing such detectors, e.g., BLASTPol, (Fissel 2013; Galitzki et al. 2014) and the SKIP concept (Johnson et al. 2014). (3) Total power detectors. These detectors – such as in SCUBA+POL-2 (Friberg et al. 2016), HAWC+ (Harper et al. 2018), or the NIKA suite of instruments (Ritacco et al. 2017) – are made capable of measuring polarization using a polarizing filter in the upstream optics. This assembly is functionally equivalent to single-polarization detectors. As a sub-category of (3), several instruments use the reflected as well as transmitted radiation from the polarizing filter, and two detectors, to measure  $I$  and one Stokes polarization parameter, similar to dual-polarization detectors. However, this approach takes up more space at the focal plane and necessitates good optical alignment to avoid effects such as differential focus. Note that none of these approaches is capable of measuring, in a single instant in time, the full Stokes vector for one point on the sky.

To recover all of  $I$ ,  $Q$ , and  $U$ , two strategies have been employed. The first is to fill the focal plane with pixels having their polarization-selective directions oriented with enough angles to fully specify the Stokes vector so that all of the information can be obtained at almost the same time, but with different pixels, by shifting the optical boresight on the sky; the second is to use a polarization rotator, i.e. a half-wave plate (HWP), to effectively rotate the incoming polarization so that all of the information can be obtained with the same pixels, but not at the same time. Use of a HWP mitigates effects such as gain errors and provides opportunity for additional signal modulation (and of the component of primary interest: the polarized one). This explains why almost all of the polarimetric instruments implemented so far, except on Planck, have introduced a rotating HWP in their optical path. Use of a HWP often comes with a need to accurately characterize “instrumental polarization.”

The PRIMAGER instrument, designed for the Probe far-Infrared Mission for Astrophysics (PRIMA; Moullet et al. 2023; Meixner et al. 2024) takes a simple ap-

proach, using single-polarization detectors oriented at three angles and no polarization modulating device. In this study, we demonstrate through simulations that the instrument and observatory designs allow total intensity and polarization to be measured with excellent sensitivity as a result of scanned observations. The Kinetic Inductance Detectors (KIDs, Baselmans et al. 2022) in PRIMAGER, operating at the background limit for a cryogenic telescope, enable the driving polarimetric science case of PRIMA – deep polarimetric mapping of nearby galaxies – even in the presence of worst-case levels of  $1/f$  noise in the detectors.

This paper is organized as follows. In Section 2, we give further detail on the design with which PRIMA intends to measure polarization and the fundamental measurement requirements. Section 3 details the algorithm for processing PRIMAGER detector samples to produce maps of intensity and polarization. Section 4 describes an end-to-end simulation of example PRIMA polarization observations and analyzes the output products. Sections 5 and 6 address certain optical design requirements and calibrations in support of PRIMA polarimetry, and finally Section 7 summarizes the key results of this study.

## 2. FAR-IR CONTINUUM POLARIMETRY WITH PRIMA

PRIMA will feature a 1.8 m diameter, cryogenic telescope delivering a field of view of  $42' \times 24'$  to its multi-wavelength, broad-band ( $R = \lambda/\Delta\lambda = 4\text{--}10$ ) mapping instrument PRIMAGER. The PRIMAGER Polarimetric Imager (PPI) half of the instrument offers four focal plane detector arrays operating simultaneously with  $R \approx 4$  centered at  $\lambda = 91, 125, 165,$  and  $232 \mu\text{m}$ . Each detector array has an instantaneous field of view of  $\sim 4' \times 4'$ . Two mapping modes are foreseen for PRIMAGER: for objects smaller than the telescope field of view, a beam-steering mirror (BSM) moves the instrument field of view within the telescope field of view, while for degree-sized fields, a combination of scanning with the observatory and the BSM will be employed.

The BSM inherits from a similar device operating on Herschel/PACS (Krause et al. 2006). It is a two-axis mirror allowing full exploration of the telescope field of view in any direction. The current design of the BSM allows for a maximum speed of  $1000''/\text{s}$  on the sky and maximum acceleration of  $10,000''/\text{s}^2$ . The BSM also hosts a location for an internal calibration source that is used to track detector gain variations during operations and to calibrate detector nonlinearity, as was done for Herschel/SPIRE (Bendo et al. 2013).

The focal plane arrays consist of KID detector pixels, where each pixel is the combination of a KID and a microlens that focuses the incoming light on the collecting or absorbing element of the detector. Pixels are arranged in a hexagonal pattern, achieving maximum packing, and the optical design is such that an  $F\lambda$  sampling is realized. A single pixel is sensitive to a single polarization direction; therefore to sample the polarization information completely, pixels sensing three different orientations, each rotated from the other by  $120^\circ$ , are placed in the focal plane, in a mixed pattern.

The PRIMA approach to polarimetry is most similar to BLASTPol (Fissel 2013; Galitzki et al. 2014), with two differences: 1) PPI uses three polarization angles in each detector array, instead of two, to allow measurement of  $(I, Q, U)$  in single scans; 2) PPI omits the half-wave plate used in BLASTPol. Located near Sun-Earth Lagrange Point 2, PRIMA should have excellent thermal stability and therefore sufficient stability in detector gain to permit effective differencing over  $\sim$ hour-long observations. The temporal stability of background power — dominated by astrophysical sources — as well as the scan modulation provided by the BSM eliminate the need for additional HWP modulation. An internal calibration source is used periodically to maintain this gain stability for the duration of the mission.

The capabilities of PPI are well-suited to making polarimetric maps of nearby galaxies. Total intensity surveys undertaken by Herschel, e.g., the Key Insights on Nearby Galaxies: A Far-Infrared Survey with Herschel (KINGFISH, Kennicutt et al. 2011) and the Herschel Reference Survey (HRS, Boselli et al. 2010), demonstrate the availability of large ( $\gtrsim 20$  arcmin<sup>2</sup>) nearby galaxies spanning a range of metallicities and star formation rates that have bright FIR dust emission. In the KINGFISH sample, Aniano et al. (2020) found that they could recover emission from galaxies down to a typical surface brightness limit of  $1.6 L_\odot \text{pc}^{-2}$ , or roughly 1 MJy/sr at  $250 \mu\text{m}$ . As resolved observations of nearby galaxies with SOFIA/HAWC+ reveal polarization fractions of order a few percent (Lopez-Rodriguez et al. 2022), this translates to roughly 0.03 MJy/sr of polarized intensity in the faintest pixels (though we note that faint regions often have higher polarization fractions, see, e.g., Jones et al. 1992; Planck Collaboration Int. XIX 2015; Lopez-Rodriguez et al. 2022). Dust models predict ratios in the dust polarization fraction between 232 and  $91 \mu\text{m}$  ranging from nearly one to factors of two or more (Draine & Fraisse 2009; Guillet et al. 2018; Hensley & Draine 2023; Ysard et al. 2024). High-signal-to-noise measurements of the polarization

fraction ( $\sigma(p) \lesssim 0.5\%$ ) at multiple frequencies promise strong discrimination among them.

### 3. POLARIZATION MAP RECONSTRUCTION

#### 3.1. Overview

The functional requirement of PPI is to make spatially resolved maps of Stokes  $I$ ,  $Q$ , and  $U$  (total and linearly-polarized intensity) in multiple far-infrared bands. Like past far-IR/(sub)mm missions that use scanning to map the sky (e.g., Griffin et al. 2010; Poglitsch et al. 2010; Tauber et al. 2010), PPI senses intensity by recording the change in power absorbed in each detector as its far-field beam is swept across the observational target. For polarization-sensitive detectors such as in PPI, the three Stokes parameters  $I$ ,  $Q$ , and  $U$  contribute to the observed signal, so a single scan with a single detector is not sufficient to uniquely distinguish the terms. At a minimum, three scans with detector(s) oriented at three well-separated polarization angles are required. In practice, PPI covers each pixel in the target mapping region with highly redundant measurements; in that region,  $I$ ,  $Q$ , and  $U$  are well determined, and many measurements are used to average down photon and detector noise. Below, we describe a least-squares approach to combining the measurements to generate spatial maps of  $I$ ,  $Q$ , and  $U$ .

The Kinetic Inductance Detectors (KIDs) in PPI do not have a clear reference to the (hypothetical) case of zero input radiation power, similar to the situation for bolometers (e.g., SPIRE 2016). The KID signal resides on an electronic “baseline” which is not of astrophysical interest but must be removed to generate sensitive maps. The detector baselines are independent and large, so an important role of the map maker is to “destripe” the maps by adjusting the subtracted baselines to minimize the variance of the redundant measurements. Destriping is most effective when scans are “crosslinked,” utilizing multiple directions crossing at  $\gtrsim 30^\circ$  angles. Due to the nonzero baselines for zero input power, PPI measures only *relative*  $I$ ,  $Q$ , and  $U$  over the mapped area, and a post-processing step is needed to set the absolute additive flux density reference, typically using the edge of the mapped area.

#### 3.2. Signal Model

Consider a position  $p$  on the sky at which there is an astrophysical signal characterized by the Stokes vector  $(I_p, Q_p, U_p)$ . The response  $S$  of a detector with gain  $g$ , polarization efficiency  $\epsilon$ , and polarization orientation  $\theta$  to this signal is (see, e.g., Kurki-Suonio et al. 2009)

$$S_{j,k} = g\{I_p + \epsilon[Q_p \cos 2(\theta - \phi_j) + U_p \sin 2(\theta - \phi_j)]\} + b_j + n_{j,k} \quad (1)$$

where the indices  $j$  and  $k$  indicate the scan number and sample number, respectively;  $\phi_j$  is the line-of-sight rotation angle of the instrument, which we assume is constant over a single scan;  $b_j$  is the electronic baseline of the detector signal; and  $n_{j,k}$  is the noise timestream.

The detector gain is assumed to be linear and constant in time either as a natural behavior of the detector, or, more likely, as a result of separate gain characterization, tracking, and correction. The detector polarization response, characterized by  $\epsilon$  and  $\theta$ , should be intrinsically time stable and is assumed to be known from ground testing. We have assumed for now that  $I$ ,  $Q$ , and  $U$  represent the convolution of the astrophysical signal with the instrument angular response and are solely dependent on position  $p$ . In Section 6, we consider detector-dependent variations in  $I_p$  which arise from variations in instrument optics.

The noise  $n$  has an expectation value of zero. We define the noise weight  $1/\sigma^2$  based on  $n$ . For white noise,  $\sigma_j^2 \equiv \langle n_j^2 \rangle$ .

### 3.3. Least-squares solution for $(I, Q, U)$

The map maker demonstrated here operates by iteratively performing a least-squares solution first for the  $I$ ,  $Q$ , and  $U$  maps given assumed detector baselines, and then the baselines given assumed  $(I, Q, U)$  maps. The latter step is discussed in Section 3.4. For the former, Equation 1 is the basis of the least-squares fit for each pixel  $p_0$  in the map. Summing over all detectors  $i$ , scans  $j$ , and samples  $k$  that observe  $p$ , the associated  $\chi^2$  of the estimated  $(I_{p_0}, Q_{p_0}, U_{p_0})$  is

$$\chi^2 = \sum_{p_i, j, k = p_0} \frac{1}{\sigma^2(S_{i,j,k})} [S_{i,j,k} - b_{i,j} - g_i(I_{p_0} + \epsilon_i[Q_{p_0} \cos 2(\theta_i - \phi_j) + U_{p_0} \sin 2(\theta_i - \phi_j)])]^2 \quad (2)$$

Minimization of  $\chi^2$  leads to coupled equations:

$$\begin{pmatrix} \sum_{p=p_0} \frac{g_i^2}{\sigma^2(S_{i,j,k})} & \sum_{p=p_0} \frac{g_i^2 \epsilon_i \cos 2(\theta_i - \phi_j)}{\sigma^2(S_{i,j,k})} & \sum_{p=p_0} \frac{g_i^2 \epsilon_i \sin 2(\theta_i - \phi_j)}{\sigma^2(S_{i,j,k})} \\ \sum_{p=p_0} \frac{g_i^2 \epsilon_i \cos 2(\theta_i - \phi_j)}{\sigma^2(S_{i,j,k})} & \sum_{p=p_0} \frac{g_i^2 \epsilon_i^2 \cos^2 2(\theta_i - \phi_j)}{\sigma^2(S_{i,j,k})} & \sum_{p=p_0} \frac{g_i^2 \epsilon_i^2 \cos 2(\theta_i - \phi_j) \sin 2(\theta_i - \phi_j)}{\sigma^2(S_{i,j,k})} \\ \sum_{p=p_0} \frac{g_i^2 \epsilon_i \sin 2(\theta_i - \phi_j)}{\sigma^2(S_{i,j,k})} & \sum_{p=p_0} \frac{g_i^2 \epsilon_i^2 \cos 2(\theta_i - \phi_j) \sin 2(\theta_i - \phi_j)}{\sigma^2(S_{i,j,k})} & \sum_{p=p_0} \frac{g_i^2 \epsilon_i^2 \sin^2 2(\theta_i - \phi_j)}{\sigma^2(S_{i,j,k})} \end{pmatrix} \begin{pmatrix} I_{p_0} \\ Q_{p_0} \\ U_{p_0} \end{pmatrix} = \begin{pmatrix} \sum_{p=p_0} \frac{g_i(S_{i,j,k} - b_{i,j})}{\sigma^2(S_{i,j,k})} \\ \sum_{p=p_0} \frac{g_i \epsilon_i \cos 2(\theta_i - \phi_j)(S_{i,j,k} - b_{i,j})}{\sigma^2(S_{i,j,k})} \\ \sum_{p=p_0} \frac{g_i \epsilon_i \sin 2(\theta_i - \phi_j)(S_{i,j,k} - b_{i,j})}{\sigma^2(S_{i,j,k})} \end{pmatrix} \quad (3)$$

Some idealized cases are helpful for turning Equation 3 into guidance for instrument design. Consider a simplified situation with uniform detector noise  $\sigma(S_{i,j,k})$ , gain  $g_i$ , and polarization efficiency  $\epsilon_i$ ; and where the observing method and map making allow the baselines  $b_{i,j}$  to be measured and subtracted with negligible noise contribution. As a first special case of that, assume that the focal plane layout and observing method produces a nearly random distribution of angles  $\theta_i - \phi_j$ . Therefore,  $\langle \cos 2(\theta_i - \phi_j) \rangle \approx 0$ ,  $\langle \cos^2 2(\theta_i - \phi_j) \rangle \approx \frac{1}{2}$ , etc.,

resulting in the following simplified solutions:

$$I_{p_0} \approx g^{-1} \langle S_{i,j,k} \rangle_{p=p_0} \quad (4)$$

$$Q_{p_0} \approx 2g^{-1} \epsilon^{-1} \langle \cos 2(\theta_i - \phi_j) S_{i,j,k} \rangle_{p=p_0} \quad (5)$$

$$U_{p_0} \approx 2g^{-1} \epsilon^{-1} \langle \sin 2(\theta_i - \phi_j) S_{i,j,k} \rangle_{p=p_0} \quad (6)$$

and associated uncertainties:

$$\sigma(I_{p_0}) \approx g^{-1} N_{p=p_0}^{-1/2} \sigma(S_{i,j,k}) \quad (7)$$

$$\sigma(Q_{p_0}) \approx \sqrt{2} g^{-1} \epsilon^{-1} N_{p=p_0}^{-1/2} \sigma(S_{i,j,k}) \quad (8)$$

$$\sigma(U_{p_0}) \approx \sqrt{2} g^{-1} \epsilon^{-1} N_{p=p_0}^{-1/2} \sigma(S_{i,j,k}) \quad (9)$$



i.e.,  $\sigma(Q_{p0}) \approx \sigma(U_{p0}) \approx \sqrt{2}\epsilon^{-1}\sigma(I_{p0})$ .  $N_{p=p_0}$  is the number of observations of position  $p_0$ .

As a second special case of uniform  $\sigma(S_{i,j,k})$ ,  $g_i$ , and  $\epsilon_i$ , consider an observation at fixed instrument rotation angle  $\phi_j$  using detectors divided evenly among three polarization angles  $\theta_i$  separated by  $60^\circ$  (or  $120^\circ$ ); this describes the intent of PPI (Section 4.1). It is straightforward to show that the Stokes vector solution and uncertainties are the same as in the random case (Equations 4-9). Furthermore, this is also the case for four or more polarization orientations equally distributed over  $180^\circ$ . This means that there is no signal-to-noise disadvantage for using the minimum number of three angles.

As discussed by Kurki-Suonio et al. (2009), the condition of the  $3 \times 3$  matrix on the left-hand side of Equation 3 is a figure of merit for the quality of the  $(I, Q, U)$  measurement in the pixel of interest. A larger determinant means a lower uncertainty in the solution. In this paper, we use the term ‘‘Stokes hits’’ for the cube root

of the determinant of the  $3 \times 3$  matrix when  $\sigma^2(S_{i,j,k})$  and  $g$  are set to unity. For the simplified case in Equations 4-9, we can recognize  $N_{p=p_0}$  as the ‘‘hits’’ for total intensity measurement. In that same case, the ‘‘Stokes hits’’ works out to  $2^{-2/3}\epsilon^{4/3}N_{p=p_0}$ , up to 63% of the total intensity hits.

### 3.4. Map Destriping and Detector 1/f Noise

For the observing mode that will be discussed and simulated in Section 4, the observation sequence is clearly divided into discrete scans, and it is natural to divide the detector timestreams into segments (one per scan) and to fit a detector baseline for each segment. With the condition that one scan corresponds to one pass over the observed source, and the additional condition that only a constant baseline is fit per detector and per scan, then the only filtering of spatial modes that occurs is removal of a constant value over the map. The least-squares solution for the baselines, given the estimate of the Stokes parameter maps, is straightforward:

$$b_{i,j} = \left( \sum_k \frac{1}{\sigma^2(S_{i,j,k})} \right)^{-1} \sum_k \frac{S_{i,j,k} - g_i(I_{p(i,j,k)}) + \epsilon_i[Q_{p(i,j,k)} \cos 2(\theta_i - \phi_j) + U_{p(i,j,k)} \sin 2(\theta_i - \phi_j)]}{\sigma^2(S_{i,j,k})} . \quad (10)$$

Subtracting baselines on each scan segment separately is an effective way to remove  $1/f$  noise from the detector signals on timescales longer than the scan duration (Figure 1; e.g., Kurki-Suonio et al. 2009).

Expanding on the mention in Section 3.1 of arbitrary value of the zero level in the output maps, we can now describe this in terms of the signal model. If one expands Equation 2 to sum over all of the positions  $\{p\}$  in the map, then attempts to solve for all  $(I, Q, U)$  and  $\{b\}$  simultaneously, then one encounters a singular matrix and degeneracy among certain parameter combinations. Specifically, if the substitutions  $b_{i,j} \rightarrow b_{i,j} - g_i \Delta I$  and  $I_p \rightarrow I_p + \Delta I$  are made for the solutions, then the value of  $\chi^2$  is unchanged, i.e., changing  $I$  by a constant amount over the full map (with a corresponding change in baselines) does not degrade the goodness of fit. Fortunately, the degeneracy exists only for the spatially-constant term. In addition to  $I$ , the degeneracy exists for the two constant terms in polarization also; for example, the substitutions  $b_{i,j} \rightarrow b_{i,j} - g_i \epsilon_i \cos 2(\theta_i - \phi_j) \Delta Q$  and  $Q_p \rightarrow Q_p + \Delta Q$  also do not change the value of  $\chi^2$ .

## 4. POLARIMETRY SIMULATION

To demonstrate the polarization-mapping capability of PPI, and to quantify the effect of detector  $1/f$  noise, we simulated an observation of a PRIMA science target

and carried out the map-making process described in Section 3.

### 4.1. Focal Plane Detector Array

For the simulations in this paper, we model the shortest- and longest-wavelength bands of the PRIM-Ager Polarimetric Imager: PPI1 with bandpass center at  $\lambda = 91 \mu\text{m}$  and PPI4 at  $\lambda = 232 \mu\text{m}$ . Each detector pixel consists of a hemispherical microlens which concentrates the intercepted power onto an antenna designed to be sensitive in a single linear polarization (Baselmans et al. 2022). The direction of polarization is varied in a regular way over the detector array such that the full array is sensitive to three angles of polarization separated by  $120^\circ$  with approximately equal number of detectors allocated for each direction. The power collected by each antenna is absorbed in a microwave resonator circuit with resonance frequency dependent on the input power. The PPI1 detectors are arranged on a hexagonal grid with nearest-neighbor separation of  $10''$  in the far field, and the estimated beam size is  $11''$  Full-Width-Half-Maximum (FWHM). For PPI4 (Figure 2), the detector separation is  $25''$ , and the estimated beam size is  $27''$  FWHM.

Noise in the simulation arises from two sources: the detector and photon statistics. To compute the latter,

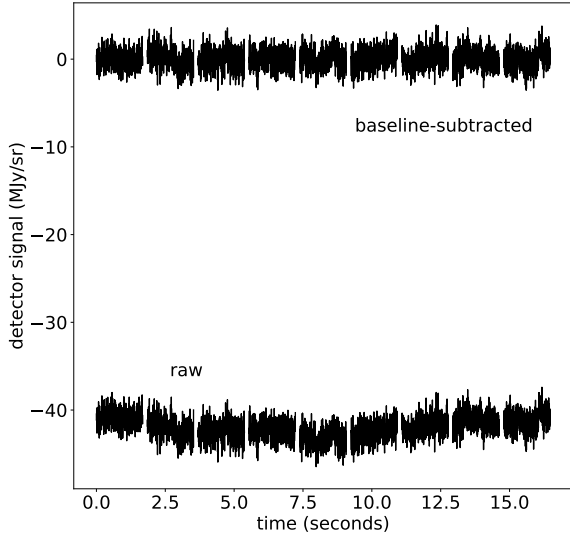


**Figure 1.** Illustration of detector  $1/f$  noise model (Section 4.1) and baseline subtraction by segments. The lower curve shows a noise model realization for one detector, for the first 16 seconds of an observation. The detectors are sampled at  $f_{samp} = 350$  Hz. The gaps in the curve are the turn-around periods between scan segments, for which the detector samples are not used in the map making. The top curve shows the detector signal after subtraction of the baselines (one for each segment) found from the iterative map solution.

the specific intensity of the source (and background)  $I_\nu$  is converted to power as follows:

$$P_{phot} = \frac{n_{pol}}{2} \eta \left( \frac{A\Omega}{\lambda^2} \right) \lambda^2 \frac{\nu}{R} I_\nu \quad (11)$$

and the Noise Equivalent Power (NEP, in  $\text{WHz}^{-1/2}$ ) is calculated as (see, e.g., Mather 1982):

$$NEP_{phot} = \sqrt{2P_{phot} h\nu} \quad . \quad (12)$$

In the prior equations,  $n_{pol}$  is the number of polarization states detected (1 for PPI),  $\eta$  is optical efficiency including the detector,  $A\Omega$  is the etendue,  $\lambda$  and  $\nu$  are the wavelength and frequency,  $P_{phot}$  is the power absorbed in the detector, and  $h$  is the Planck constant; see also Table 1. For the simulation, the photon coherence term has not been included since it makes a negligible contribution (fractional increase  $< 10^{-4}$  for NGC 6946 and PPI bands). The noise intrinsic to the detector is assumed to be independent of the photon power for the

intensity range in this paper<sup>1</sup> so a fixed  $NEP_{det}$  adds in quadrature with  $NEP_{phot}$  to give  $NEP_{tot}$ . The Noise Equivalent Intensity (NEI) for a given detector is defined as follows:

$$NEI = NEP_{tot} / \left[ \frac{n_{pol}}{2} \eta \left( \frac{A\Omega}{\lambda^2} \right) \lambda^2 \frac{\nu}{R} \right] \quad (13)$$

For low-background lines of sight with  $I_\nu = 7$  MJy/sr, and the “modeled” parameter assumptions in Table 1, the NEI for PPI1 is 0.182 MJy/sr/Hz<sup>1/2</sup>, and for PPI4 is 0.071 MJy/sr/Hz<sup>1/2</sup>. The uncertainty in a measurement of specific intensity  $I_\nu$  is related to  $NEI$  and integration time  $T$  as follows:  $\sigma(I_\nu) = \frac{NEI}{\sqrt{2T}}$  (e.g., Rieke 1996).

The simulation first generates “photon only” detector timestreams by looking up  $(I, Q, U)$  for the relevant positions on the sky and applying Equation 1. (Instrument emission and stray light are assumed negligible.) In the same loop through detectors and samples, photon noise is applied by adding a random number drawn from a gaussian distribution with mean 0 and standard deviation  $(\frac{f_{samp}}{2}) NEP_{phot}$ , where  $\frac{f_{samp}}{2}$  is the bandwidth of the detector samples.

The detector noise is modeled with a white noise component and a  $1/f^n$  component. For each detector and for the full period of time required to complete one repetition of the scan pattern, a long timestream is modeled using the prescription in the prior sentence for the power spectral density, along with randomized phases. Each repetition of the scan pattern is modeled independently. The detector noise timestream is added to the “photon only” timestream, which is then added to a large, random baseline constant over the repetition. Measurements of prototype PRIMAGER KIDs (similar to those reported by Baselmans et al. 2022) indicate a  $\sim 1/f^{0.6}$  spectrum; in the simulations, the amplitude of this component has been exaggerated by a factor of  $\sim 10$  to examine robustness of the observation approach to noise of this type.

For simplicity, the simulation uses uniform weighting – constant  $\sigma^2(S_{i,j,k})$  – for all detectors contributing to a map pixel. This approximates the case of a focal plane with a small distribution of detector noise properties. Since we are not yet in the situation of correcting for a distribution of detector gains and polarization efficiencies, we set  $g_i = 1$  (until Section 5) and  $\epsilon_i = 0.99$  for the simulations.

<sup>1</sup> Although this assumption is not accurate in detail for KIDS (Baselmans et al. 2022), it is a reasonable approximation for the purpose of this simulation.

**Table 1.** Predicted and modeled (worst-case) PPI instrument parameters

Parameter	PPI1 predicted	PPI1 modeled	PPI4 predicted	PPI4 modeled	Unit
$NEP_{det}$ (white comp.)	$\leq 3.0 \times 10^{-19}$	$6.0 \times 10^{-19}$	$\leq 3.0 \times 10^{-19}$	$6.0 \times 10^{-19}$	$\text{W Hz}^{-1/2}$
$NEP_{det}$ (1/f comp.)	$\leq 6.0 \times 10^{-20} \left(\frac{f}{10\text{Hz}}\right)^{-0.6}$	$6.0 \times 10^{-19} \left(\frac{f}{10\text{Hz}}\right)^{-0.6}$	$\leq 6.0 \times 10^{-20} \left(\frac{f}{10\text{Hz}}\right)^{-0.6}$	$6.0 \times 10^{-19} \left(\frac{f}{10\text{Hz}}\right)^{-0.6}$	$\text{W Hz}^{-1/2}$
optical efficiency $\eta$	0.29	0.15	0.29	0.15	
detector $A\Omega/\lambda^2$	0.74	0.74	0.74	0.74	
polarization efficiency $\epsilon$	$> 0.99$	0.99	$> 0.99$	0.99	
NEI (7 MJy/sr bgnd.)	0.077	0.182	0.030	0.071	$\text{MJy/sr/Hz}^{1/2}$
sample yield <sup>a</sup>	$\geq 0.92$	0.90	$\geq 0.92$	0.90	
detector yield	$\geq 0.80$	0.80	$\geq 0.80$	0.80	

NOTE—<sup>a</sup>Due to cosmic rays

To simulate a focal plane with imperfect yield, 20% of the detectors have been omitted from the simulation randomly (Figure 2). To simulate the data loss from cosmic rays, 10% of the detector samples are omitted randomly. This is a conservative estimate, as we expect losses of between 2% and 8% based on scaling from laboratory measurements of representative KIDs (Kane et al. 2024), and assuming simple masking of the impacted timestream. Cosmic ray processing is done on board, with a base sample rate of 10 kHz, prior to rebinning to 350 Hz for downlink. The data loss may be reduced by subtracting the tails of the events, as was done with Planck (Catalano et al. 2014), but in the on-board electronics in the case of PRIMA. We found from simulation that the only significant impact of the omission of samples from the mapping is the loss of integration time.

#### 4.2. Simulated Science Target

As an illustrative test case of our polarimetric mapping techniques, we consider a mock observation of the nearby face-on spiral galaxy NGC 6946. Its FIR size of 100 arcmin<sup>2</sup> (Aniano et al. 2020) is well-matched to mapping with PPI while a wealth of ancillary data, including FIR and radio imaging and polarimetry, can inform our signal model. Although we hew closely to available data where possible, for the purposes of this work we prioritize a signal model that best illustrates PPI mapmaking capabilities and limitations rather than a strict forecast; we note our simplifying assumptions below.

Our PPI1 simulations are based on 100  $\mu\text{m}$  observations with the Herschel/PACS instrument (ESA Herschel Science Archive, OBSIDs 1342191947-50). These data have an angular resolution of 7'' and a pixel size of 1.6''. We first smooth the map to a PPI1 resolution of 11'' with a pixel size of 3'' using the `astropy reproject`

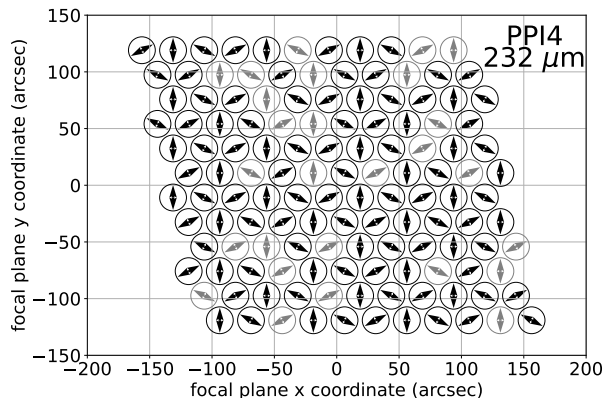


**Figure 2.** Focal plane layout of PPI4. 132 microlens-fed kinetic inductance detectors are arranged in a hexagonal-close-packed configuration with nearest-neighbor spacing of 25'' on the sky. The arrows show the direction of sensing linear polarization for each detector, dictated by the KID antenna design. Three polarization angles are distributed evenly through the focal plane. The detectors shown in gray were omitted (by random number generation) from the mapping simulations to capture the worst-case detector yield. PPI1 has 1116 detectors arranged in a similar pattern with 10'' nearest-neighbor separation.

package. We extract a 350×350 pixel region centered on the nucleus for our fiducial Stokes  $I$  map to avoid noise at the edges of the PACS map. For simplicity, we adopt the flux densities as-is, i.e., without accounting for the slightly shorter wavelength of PPI1.

Our PPI4 simulations are based on 250  $\mu\text{m}$  observations with the Herschel/SPIRE instrument (ESA Herschel Science Archive, OBSIDs 1342183046-53, 1342183364, 1342183366, 1342188786, 1342266676). Unlike the PACS map, the SPIRE map has an overall zero level of approximately 12.2 MJy sr<sup>-1</sup>, which we re-

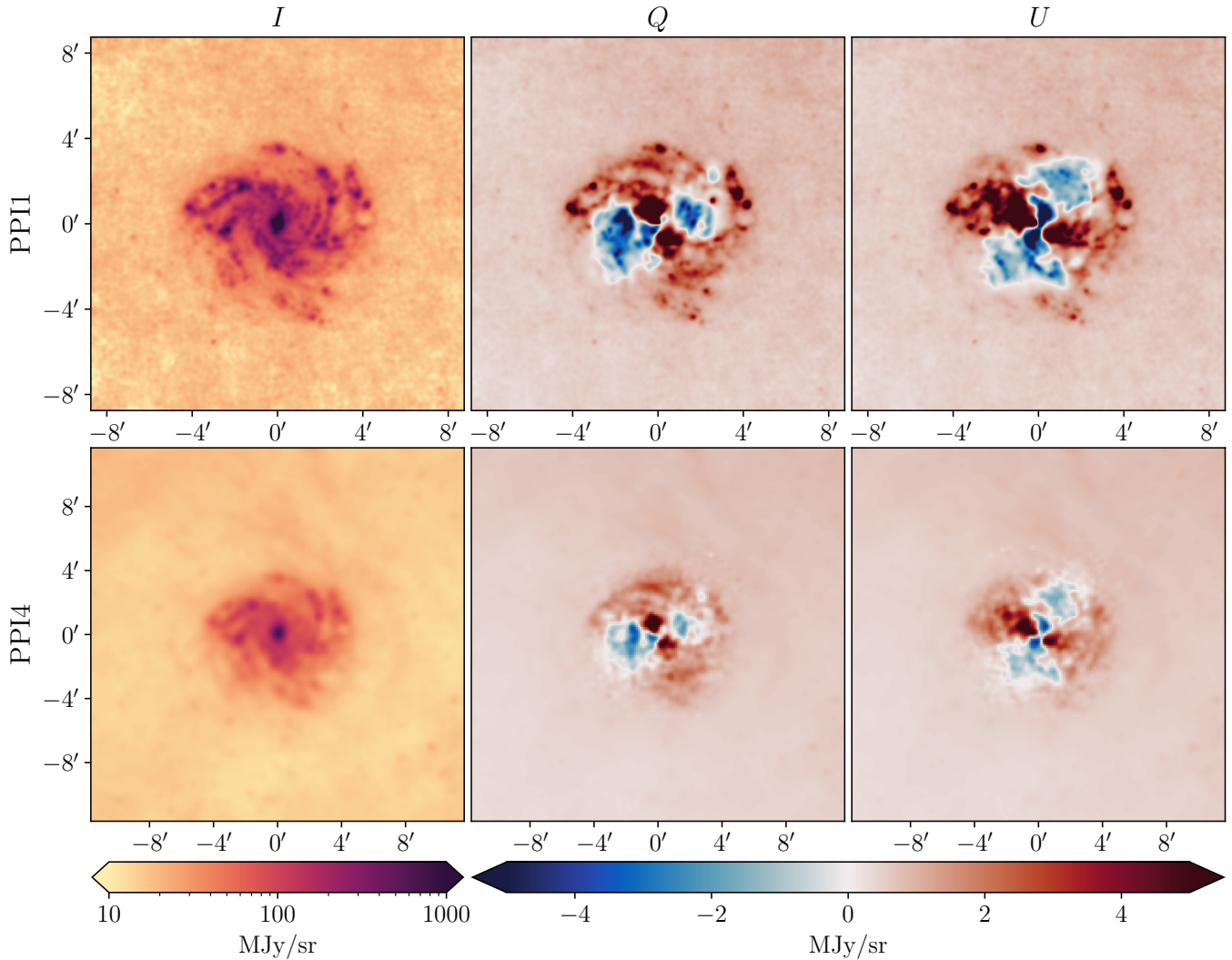


**Figure 3.** Input “truth”  $I$  (left),  $Q$  (middle), and  $U$  (right) maps for PPI1 (top) and PPI4 (bottom) derived from Herschel and VLA observations as described in Section 4.2. By choice of the cirrus model, the  $Q$  and  $U$  “foreground” emission at the periphery of the maps is positive.

move for our initial processing. The SPIRE map has an angular resolution of  $17''$  and has  $6''$  pixels. We smooth to a PPI4 resolution of  $27''$  and a pixel size of  $7''$ . We extract a  $400 \times 400$  pixel region centered on the nucleus for our fiducial Stokes  $I$  map. As with the PPI1 map, we do not attempt to correct for the small wavelength difference between PPI4 and Herschel and so use the measured flux densities as-is.

For the Stokes  $Q$  and  $U$  maps, we start from 6 cm observations of NGC 6946 with the Very Large Array<sup>2</sup> (Borlaff et al. 2023). While the polarized intensity of

the synchrotron emission measured at 6 cm is unlikely to be strongly correlated with dust polarization at shorter wavelengths, the orientation of the galaxy-scale magnetic field as probed by these tracers should be similar. Therefore, we adopt the polarization angles of the radio data. We make the additional assumption that the synchrotron polarization fraction is perfectly correlated with the dust polarization fraction. While unlikely to be true in practice, this provides a straightforward means of inducing polarization fraction variations across the map. We reduce the radio polarization fraction by a factor of three to account for the fact that the intrinsic dust polarization fraction is less than that of synchrotron emission. The resulting distribution of polarization fractions is broadly consistent with FIR measurements of nearby galaxies (Lopez-Rodriguez et al. 2022).

<sup>2</sup> FIR  $Q$  and  $U$  maps of NGC 6946 were made with SOFIA (Borlaff et al. 2023), but these maps have lower signal-to-noise ratio over less area of the galaxy than the radio data and so are less suitable for simulation purposes.



Explicitly, the PPI1 and PPI4  $Q$  and  $U$  maps are constructed from the radio  $Q_R$  and  $U_R$  maps, the PPI1 and PPI4  $I$  maps, and the radio  $I_R$  map as

$$Q_{\text{PPIX}} = 0.33 I_{\text{PPIX}} \frac{Q_R}{I_R} \quad (14)$$

$$U_{\text{PPIX}} = 0.33 I_{\text{PPIX}} \frac{U_R}{I_R} \quad (15)$$

where X denotes either 1 or 4.

While the radio data provide a constraint on the magnetic field morphology across the disk of NGC 6946, they do not probe the foreground Galactic cirrus that is evident in both Herschel maps. To account for the cirrus, we first construct an ansatz cirrus polarization fraction map that smoothly varies from 0% in the southeast corner of the map to a value approaching 10% in the northwest corner, consistent with observed values of Milky Way cirrus across the sky (Planck Collaboration Int. XIX 2015). This variation is not necessarily physical nor based on data (e.g., from Planck), but rather is a means of introducing variable polarization fractions into the simulations. We assume that the cirrus has equal power in  $Q$  and  $U$  to construct the final cirrus  $Q$  and  $U$  maps from our cirrus polarization fraction map and the Herschel  $I$  maps. We employ an apodized mask to smoothly transition from the cirrus  $Q$  and  $U$  maps to the galaxy  $Q$  and  $U$  maps based on the radio data.

Finally, we reintroduce a zero level back into both  $I$  maps. As Galactic dust has comparable brightness at 91 and 232  $\mu\text{m}$  (e.g., Dwek et al. 1997), we employ a value of  $12.2 \text{ MJy sr}^{-1}$  at both wavelengths. Since this zero level is likely dominated by Galactic cirrus, with NGC 6946 being just  $11.7^\circ$  off the Galactic plane, we add this zero level to the  $Q$  and  $U$  maps using our cirrus polarization fraction map assuming equal power in  $Q$  and  $U$ .

The final  $I$ ,  $Q$ , and  $U$  maps for PPI1 and PPI4 are presented in Figure 3. These constitute the “ground truth” for our simulated observations.

### 4.3. Scan Pattern

To guide the choice of the scan pattern, we assume that the PPI detectors are sampled at  $f_{\text{samp}} = 350 \text{ Hz}$  and have a useful bandwidth of  $175 \text{ Hz}$ . At the PPI shortest wavelength,  $\frac{\lambda}{2D}$  Nyquist sampling of the sky is  $5.2''$ , allowing a scan rate as high as  $5.2'' \times 350 \text{ Hz} = 1820''/\text{sec}$ . For the simulations in this study, we use a scan rate of  $500''/\text{sec}$ .

PRIMA observations of science targets that are several arcminutes across, such as NGC 6946, can take advantage of the Beam-Steering Mirror (BSM). The BSM provides large scan rates along with large acceleration

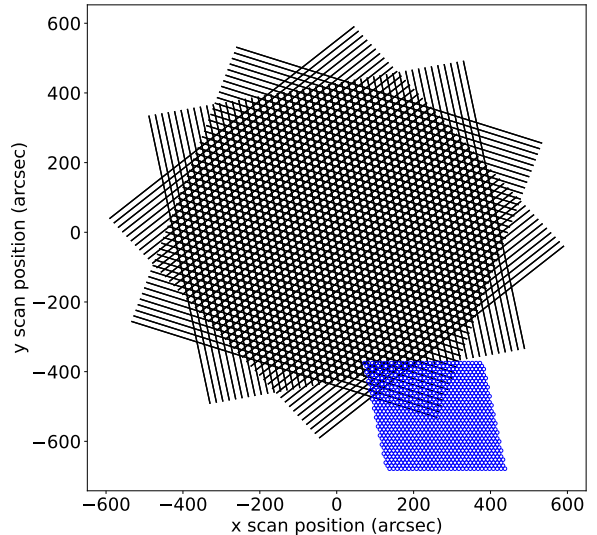


**Figure 4.** Scan pattern used in the simulation. Each of the  $3 \times 50$  black lines shows the trajectory of the center of the detector array on a Cartesian sky coordinate system. For scale, the  $31 \times 36$  layout of the PPI1 detector array is shown in blue at one of the extreme points of the scan. The observation is 1.5 hour in duration, and rotation of the field is negligible over that time given PRIMA’s L2 orbit. The scan pattern fits within a diameter of  $20'$ . Adding the footprint of the detector array, the observed area is within a  $25' \times 24'$  rectangular region.

for time-efficient scan “turn-arounds.” The PRIMA optics and BSM allow regions of  $24' \times 42'$  to be mapped without moving the bulk telescope and spacecraft.

The scan pattern simulated for this study is shown in Figure 4. Three scan axes are used, matching the three-fold symmetry of the focal plane. The exact directions were not found to be critical for successfully recovering the source Stokes vectors; however, the scan direction, along with the spacing of the raster lines, affects the uniformity of coverage. The simulation uses scan directions at a  $19.1^\circ$  angle from the focal plane symmetry axes. Each raster line is  $840''$  long (lasting 1.68 seconds) and is covered in a back-and-forth way. The spacing of the raster lines is  $17''$ . The simulation assumes that the BSM reverses the scan direction and (on half of the occasions) moves to the next raster line within 0.17 seconds, requiring an angular acceleration of the far-field beam of  $6000''/\text{sec}^2$ : within the design specifications of the BSM. There are  $3 \times 50 \times 2 = 300$  total scan segments in the scan pattern, and the pattern is repeated 10 times in the simulation, so the total observation duration is 1.5 hour.

#### 4.4. Simulation Results

Simulations were performed for multiple noise realizations of PPI1 and PPI4. Each realization used the scan pattern from Section 4.3 and Figure 4, carried out for the 10 repetitions. The target was “observed” in each band independently (although an optimized scan pattern could be enlarged to observe multiple bands simultaneously and more efficiently). From the simulated detector timestreams,  $I$ ,  $Q$ , and  $U$  maps were generated according to Equation 3, iterated with solution for the detector baselines (Equation 10). For convenience, the output map pixel scale matched the input (Section 4.2). Convergence of the iteration is driven by the settling of the adjusted baselines. For our choice to simulate baselines much larger than the astrophysical signal and  $1/f$  noise on long timescales, convergence was sped up (with no observable impact to the final maps) by first subtracting the median signal from each detector for each scan segment prior to starting the iteration. 20 iterations were sufficient for convergence, judged by monitoring of  $\chi^2$  (Equation 2) and the larger-scale patterns in the differences of output maps and input “truth” maps.

Example output maps from the simulations are shown in Figure 5. For PPI4, the median Stokes hits in the central  $10'$  diameter (left panel) is 7040 per  $7''$  pixel, which is 62% of the median total intensity hits of 11,350 (32 seconds observing time per map pixel). The ratio matches the expectation from Section 3.3 for good polarization angle coverage. The reconstructed Stokes  $I$  (center panel),  $Q$  (right panel), and  $U$  are mapped with high signal-to-noise in the central  $10'$  diameter.

The sensitivity of the maps can be quantified by taking differences of the input and output (1.5 hour observation) maps (Figure 6). Note that we have applied a zero level correction to all maps for this comparison (as discussed further in Section 4.5). For PPI4, the standard deviation of the pixels in the central  $10'$  diameter of the  $I$  difference is 0.017 MJy/sr. This is  $1.3\times$  the white-noise-only expectation of 0.013 MJy/sr based on the median  $I$  of 38 MJy/sr, 32 seconds of integration, and the equations in Section 4.1. The standard deviation of the  $Q$  (or  $U$ ) difference in the  $10'$  diameter is 0.024 MJy/sr, also  $1.3\times$  the white-noise prediction. This excess noise is due to the  $1/f^n$  noise not included in the prediction. Statistics of the multiple observational realizations indicate similar values for the sensitivity in the maps.

The photon noise from NGC 6946 and the Galactic foreground in its vicinity partially “hide” the detector  $1/f^n$  noise. To quantify this, we also performed a simulation with an input map which had spatially-uniform  $I = 7$  MJy/sr and  $Q = U = 0$ . Otherwise, the instru-

ment and observational parameters were the same as for NGC 6946. For the 1.5 hour observation, we found a per-pixel sensitivity of 0.0136 MJy/sr ( $1\sigma$ ) in Stokes  $I$  and 0.0188 MJy/sr ( $1\sigma$ ) in Stokes  $Q$  or  $U$ , both  $1.5\times$  the theoretical expectation with white noise only.

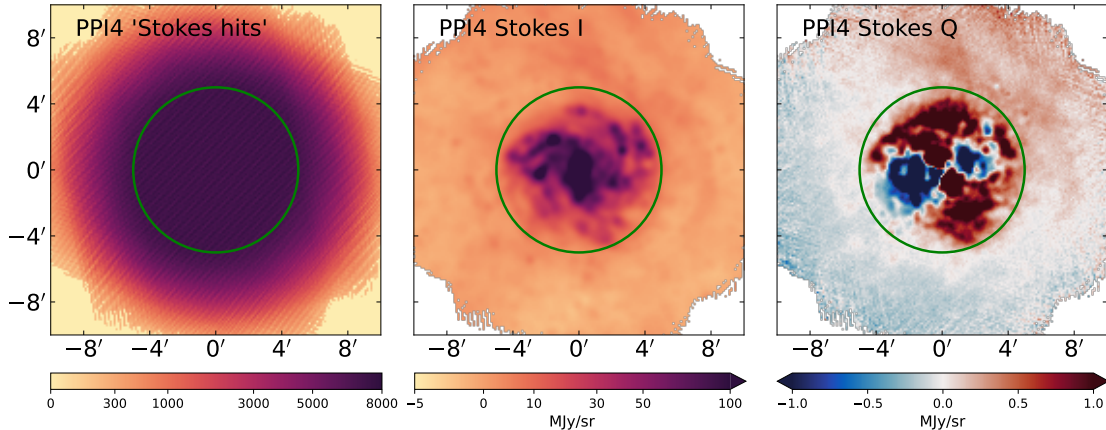
For PPI1, the median Stokes hits in the central  $10'$  diameter is 11,050 per  $3''$  pixel, which is 62% of the median total intensity hits of 17,800 (51 seconds). Based on differences of output and input maps, the per-pixel sensitivity for 1.5 hours observing, within the central  $10'$  diameter of NGC 6946, is 0.038 MJy/sr ( $1\sigma$ ) in Stokes  $I$  and 0.054 MJy/sr ( $1\sigma$ ) in Stokes  $Q$  or  $U$ . This is  $1.4\times$  the white-noise-only expectations of 0.027 and 0.039 MJy/sr, respectively, based on the median  $I$  of 44 MJy/sr and 51 seconds of integration.

Figure 7 demonstrates how the sensitivity depends on the emission from the galaxy and background. Multiple map pixels can be combined to produce higher signal-to-noise in the measurement of total or polarized intensity, as long as the small noise correlations due to  $1/f^n$  noise are taken into account (as is done in the next Section). Even though the mapped area extends over the  $24'$  width of the telescope field of view – larger than needed for a more typical KINGFISH or HRS galaxy – the sensitivity predicted from the simulation is a factor of 1.5 better than the target outlined in Section 2. For a test case with half the dimension of the scan pattern from Figure 4, we find nearly identical ( $I, Q, U$ ) maps for the galaxy but an increase of  $3.8\times$  for the integration time per pixel in the center of the map, which leads to a  $1.9\times$  improvement in sensitivity. Using the “predicted” instrument parameters rather than the “modeled” worst-case parameters in Table 1 improves the sensitivity by a further factor of  $1.5\times$ – $2.0\times$ .

#### 4.5. Analysis of Simulated Data

The first step in analyzing the simulated maps is to address the unknown zero level. Since the PPI measurements are purely differential, we follow the simplest approach of finding the constant value for each map that, when added, yields emission consistent with zero in the outskirts of the map. Specifically, we subtract from each of the  $I$ ,  $Q$ , and  $U$  maps the median value of the map within an equal-area annulus surrounding our  $10'$ -diameter analysis region. We apply the same procedure to the  $I$ ,  $Q$ , and  $U$  “truth” maps as well for all comparisons that follow.

The scientific quantities of interest can be derived straightforwardly from the  $I$ ,  $Q$ , and  $U$  maps. First, the polarization fraction  $p$  encodes the intrinsic polarization efficiency of the emitting dust grains, the inclination of the magnetic field aligning the grains, and the degree of



**Figure 5.** A selection of the outputs from one observation realization with PPI4. The left panel shows a map of “Stokes hits” (Section 3.3). The  $10'$  diameter science analysis region is shown with a green circle on all panels. The Stokes hits has a peak value of 7720 and a minimum value of 6230 within the  $10'$  diameter, for the  $7''$  pixel scale used. The  $I$  and  $Q$  images in the middle and right panels are displayed with saturated color scales to show low-level features. The faint striping at the edges of the  $Q$  map is a signature of the detector  $1/f$  noise.

disorder of the magnetic field along the line of sight. It is given by

$$p \equiv \frac{\sqrt{Q^2 + U^2}}{I} . \quad (16)$$

Because the effects of magnetic field geometry are independent of frequency, the dust composition can be constrained by observing how  $p$  varies with frequency. In general, dust models with multiple components predict strong variation of  $p$  with frequency especially near the peak of the dust emission spectrum (Draine & Fraisse 2009; Guillet et al. 2018; Draine & Hensley 2021; Ysard et al. 2024), whereas models with only one component predict little variation (Hensley & Draine 2023).

The second quantity of interest is the polarization angle  $\psi$ , which encodes the orientation of the magnetic field aligning the grains as projected onto the plane of the sky. It is given by

$$\psi \equiv \frac{1}{2} \arctan \left( \frac{U}{Q} \right) . \quad (17)$$

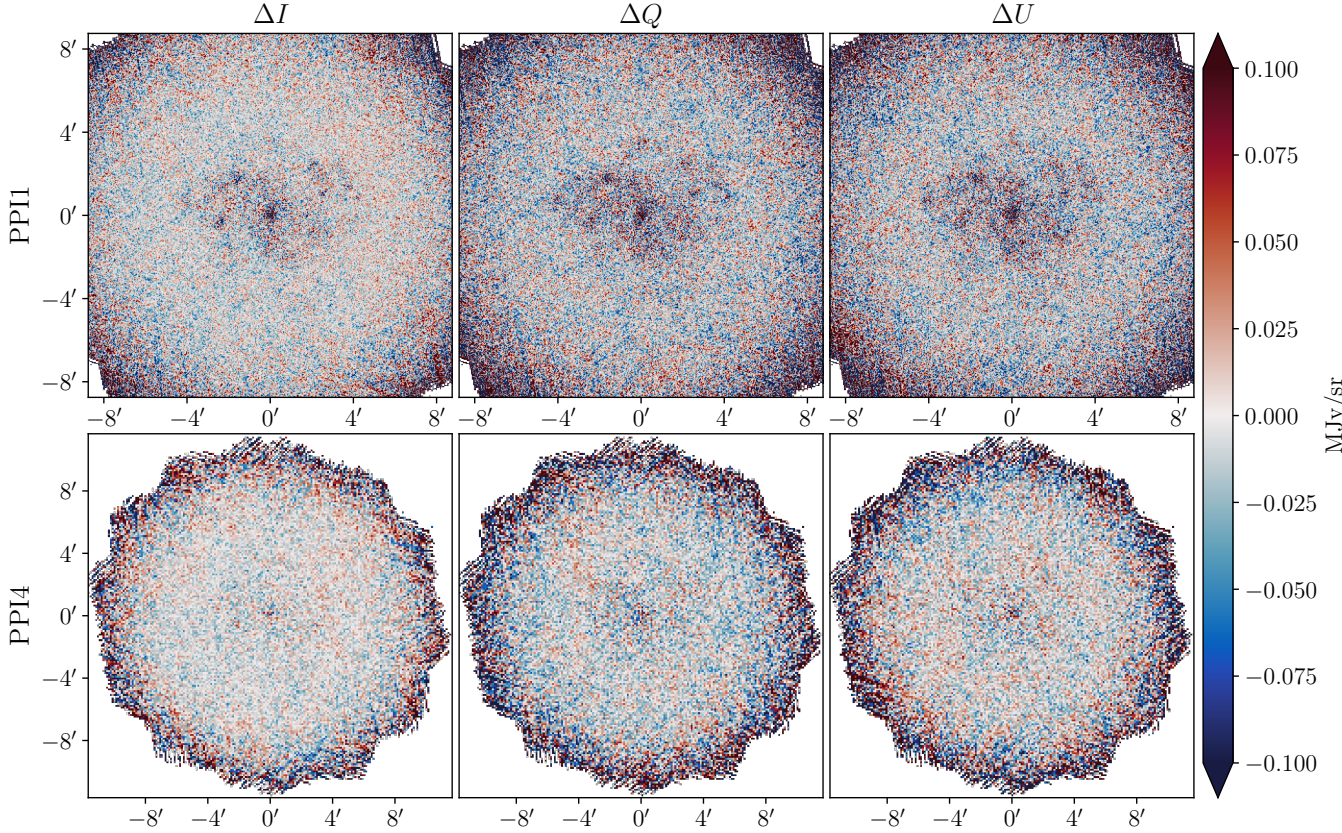
Since dust emission is polarized perpendicular to the orientation of the local magnetic field, the measured  $\psi$  must be rotated by  $90^\circ$  to correspond to magnetic field orientation. Maps of  $\psi$  reveal how magnetic fields relate to structures at all scales, while the dispersion in  $\psi$  can be used to constrain the local magnetic field strength (e.g., Planck Collaboration XII 2020). The polarization vectors of the “observed” maps are illustrated in Figure 8.

Figure 9 compares the  $p$  and  $\psi$  values in the “observed” maps to the values in the “true” map in a  $10'$  diameter circular region centered on the galaxy. While the uncertainty in  $p$  and  $\psi$  can be straightforwardly computed from the uncertainties in  $I$ ,  $Q$ , and  $U$  under the assumption of Gaussian errors, the presence of  $1/f$  noise complicates the picture. We find that 65% of observed PPI1 pixels and 76% of observed PPI4 pixels differ by less than 0.2% in  $p$  from the truth maps. For a median  $I$  of 38 MJy/sr and  $\sigma(Q) = \sigma(U) = 0.024$  MJy/sr (see Section 4.4),  $\sigma(Q)/I = 0.06\%$ , in line with the distribution of values observed here. Likewise, 58% of observed PPI1 pixels and 70% of PPI4 observed pixels differ in  $\psi$  by less than  $1^\circ$ .

Comparisons of polarization fractions and angles across frequencies in a real analysis would be performed at the resolution of PPI4, enhancing the signal-to-noise ratio of the PPI1 maps by smoothing. However, due to pixel-to-pixel covariance, the gains will not be as large as if the pixels were completely independent. We find that the per-pixel signal to noise of the PPI1 map improves by a factor of  $\sim 8$  after smoothing with a  $25''$  FWHM gaussian to match the PPI4 resolution, somewhat smaller than the naive expectation of 12.

If in the future PRIMA or a similar mission achieves the sensitivity modeled in this simulation, then it will enable polarization mapping of galaxies  $\sim 300 - 1000\times$  deeper than SOFIA (Borlaff et al. 2023). For NGC 6946 specifically, the magnetic field could be mapped, and the dust polarization spectrum measured, throughout





**Figure 6.** Difference between the “observed” map and the input signal map in each of  $I$  (left),  $Q$  (middle), and  $U$  (right) for both PPI1 (top) and PPI4 (bottom). All maps have had zero levels removed as described in Section 4.5. There is little structure in the map aside from an imprint of the galaxy where the pixel value scatter is dominated by photon noise and near the map edges where the hit count is low.

the 20 kpc disc for the first time. Smoothed to beam scale, the simulated PPI4 polarized intensity maps reach  $\sim 6$  MJy/sr, within a factor of 2-3 of the extragalactic polarized intensity background fluctuations (B  thermin et al. 2024).

## 5. RELATIVE GAIN CALIBRATION

Good calibration of the relative detector gains  $\{g_i/g_j\}$  is necessary in a case such as PPI in which multiple detectors will be used, without polarization modulation, to recover the polarization signals. First, we demonstrate that the relative gains can be derived from observations of an astronomical source, even if it has intrinsic polarization, as long as it is observed for three line-of-sight rotation angles separated by  $\sim 10$ 's of degrees. Absolute flux density calibration is not discussed here, so the total intensity  $I$  is divided out:

$$S_{i,j,k} = g_i I_{p(i,j,k)} [1 + \epsilon_i q_{p(i,j,k)} \cos 2(\theta_i - \phi_j) + \epsilon_i u_{p(i,j,k)} \sin 2(\theta_i - \phi_j)] \quad (18)$$

The baseline  $b$  is dropped here, presumed to have been determined and subtracted as in Section 3.4, and the observation is presumed long enough to make the noise  $n$  negligible.  $q$  and  $u$  give the fractional polarization expressed in Stokes parameters.

We consider a highly simplified observational example, consisting of two steps. First, a single source position is observed with a single detector at three rotation angles. This provides three measurements, with three unknowns: the average response  $g_1 I_{p1}$ ,  $q_{p1}$ , and  $u_{p1}$ . As long as there is sufficient range in  $\phi_j$ , the set of three instances of Equation 18 can be solved for the unknowns. Next, an additional observation of the same source position is made with a second detector. With all of the terms inside the square brackets now known, the average response  $g_2 I_{p1}$  is derived, and therefore  $g_1/g_2$ . This process could be extended to the full detector array; in practice, the relative gains will be derived iteratively with the source map and baselines over a large data set with significant line-of-sight rotation and redundant observations of a field.

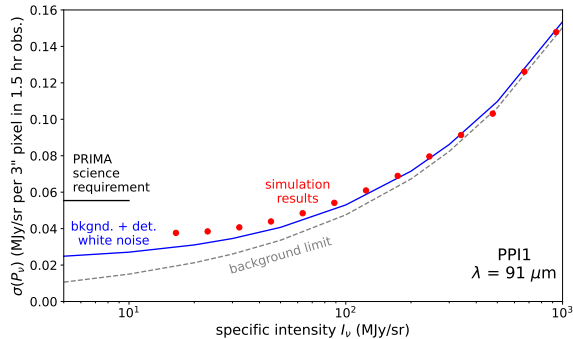


**Figure 7.** Comparison of sensitivity measured from simulated PPI1 observations and two limiting cases. The sensitivity is shown for polarized intensity  $P_\nu = \sqrt{Q_\nu^2 + U_\nu^2}$ , and the uncertainty is estimated as  $\sigma(P_\nu) \approx (\sigma(Q_\nu) + \sigma(U_\nu))/2$ . The sensitivity is measured per pixel for a 1.5 hour observation resulting in 51 sec integration time per pixel. The gray dashed line shows the theoretical sensitivity (“background limit”) for an instrument with no detector noise and an end-to-end optical efficiency of 0.15. The solid blue curve shows sensitivity including the modeled worst-case detector white noise. The red points are determined from the simulated observations, which include the modeled worst-case detector  $1/f^n$  noise. For each intensity bin, the standard deviation is computed for the difference of output and input maps. The sensitivity is compared to the PRIMA polarimetry science requirement of  $5\sigma = 0.030$  MJy/sr in 2 hr, converted from PPI4 beam area to  $3''$  pixels as described in Section 4.5. The simulated map sensitivity is better than the requirement, despite the pessimistic assumptions about the instrument captured in Table 1 and the large,  $24'$  coverage of the scan pattern which could be concentrated for smaller targets. (See discussion at the end of Section 4.4 .)

Line-of-sight rotation for PRIMA is achieved by re-observing a target some number of days, weeks, or months later. The PRIMA Sun/Earth/Moon avoidance constraints permit only modest rotation for sources at low ecliptic latitude. However, targets within  $10^\circ$  of the ecliptic poles are continuously viewable and can be observed with full rotation of the field. The Large Magellanic Cloud is  $5^\circ$  from the south ecliptic pole and is bright and extended in the far infrared (Meixner et al. 2013), making it an excellent candidate for PPI relative gain calibration. To ensure that the detector system gain is stable over multiple, rotated observations, measurements are made of the internal calibration source, designed to produce a temporally-constant illumination over similarly long periods.

An error in relative gain for a detector will leave an imprint (positive or negative) in the  $Q$  and/or  $U$  maps, proportional to Stokes  $I$ . For a reference polarization systematic error limit of 0.5%, the relative gains need to

be known to better than  $\sim 0.7\%$  accuracy for measurement with a minimum number of detectors. However, this systematic effect averages down as more detectors with uncorrelated gain errors measure a given point on the sky. Relative gain errors can also lead to errors in the baseline determination and therefore low-level but undesirable stripes in the maps radiating from brighter sources. These are reduced by setting an upper intensity limit for samples which are used in the baseline fits.

To assess the calibration accuracy requirement for PPI, we performed a PPI1 observation simulation as described in Section 4, but this time introducing relative gain error, implemented as a gaussian random distribution over the detectors with mean of 1 and standard deviation of 0.05. We evaluated results by performing comparison of polarization fraction  $p$  and angle as in Figure 9, with the difference now being for the simulation with gain error vs. one with no gain error. We find that even with the 5% ( $1\sigma$ ) gain error as described, the  $1\sigma$  error in  $p$  is still  $<0.5\%$  .

## 6. POINTING AND BEAM MATCHING REQUIREMENTS

In this last section, we outline systematic effects related to matching of detector beams (spatially or temporally) and how they are addressed in PPI observations. In all cases, the primary concern is conversion of total intensity  $I$  into an erroneous, artifact  $Q$  or  $U$  with a spatial dependence.

First, we consider the relative pointing knowledge requirement. In the single-polarization detector approach such as in PPI, the detector differencing to measure polarization is not done with simultaneous measurements, so a drift in pointing between the measurements can lead to a residual in the polarization. In the limit of bounded pointing error and many redundant measurements, the residual will tend to average down with time, with degraded image resolution becoming the lasting effect.

For observation of an unpolarized, unresolved source, pointing displacement by  $\sim 0.005$  beam FWHM causes a 0.5% residual in the polarized intensity map (Figure 10), which sets a relative pointing knowledge target for the observations. At the wavelength of PPI1, this is  $0.06''$ .

Error in the pointing information provided in the PRIMA telemetry can be lessened by using the PPI measurements themselves to make corrections. This technique has been demonstrated qualitatively by, e.g., Stone et al. (2016) using Herschel/SPIRE imaging at 250–500  $\mu\text{m}$ . It is difficult to forecast the kind of pointing error that PPI will experience; potentially,  $\sim 4$  additional fit parameters could be added per raster line, to correct starting position and velocity.



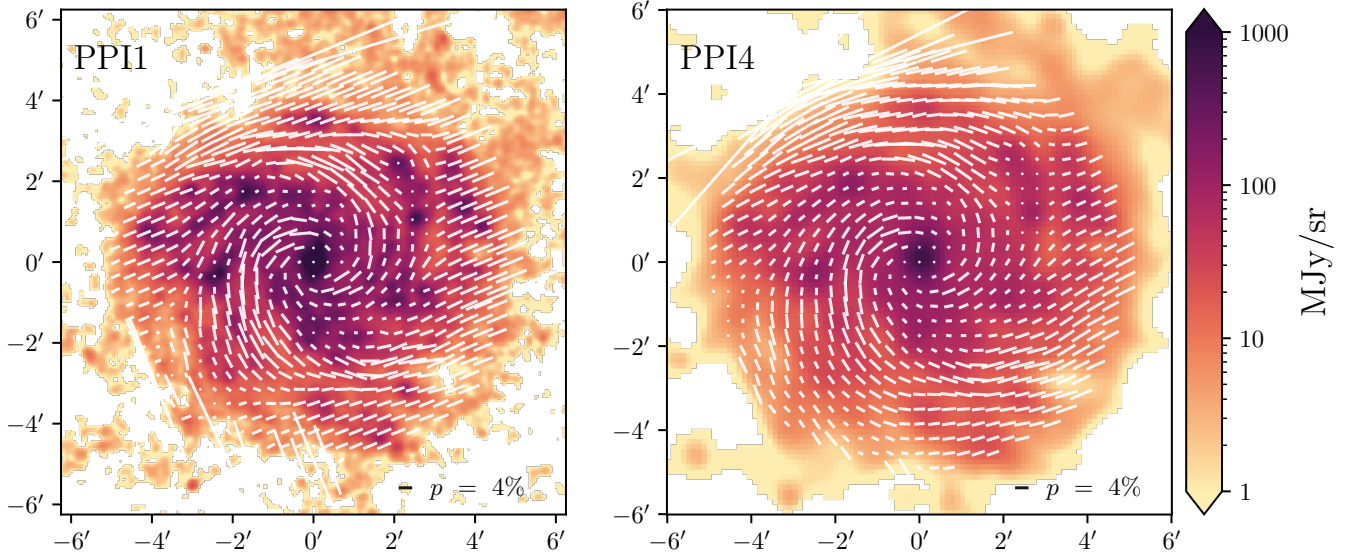


**Figure 8.** The “observed” polarization vectors corresponding to magnetic field orientation (i.e.,  $\psi$  rotated by  $90^\circ$ ) are overlaid on the “observed” total intensity maps for PPI1 (left) and PPI4 (right). For visual clarity, one vector in the PPI1 map is an average over a  $7 \times 7$  pixel region (i.e.,  $21'' \times 21''$ ) while one vector in the PPI4 map corresponds to a  $3 \times 3$  pixel region (i.e.,  $21'' \times 21''$ ). The vector length is proportional to the polarization fraction.

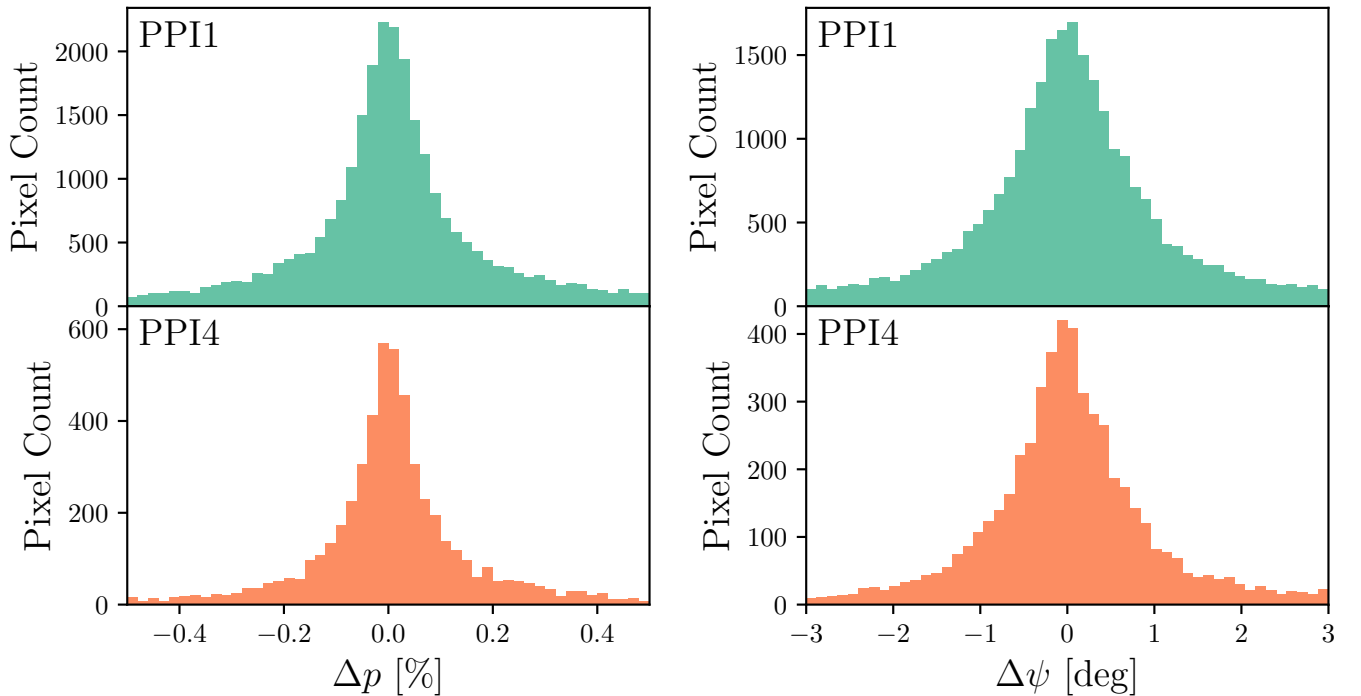


**Figure 9.** The difference in polarization fraction ( $\Delta p$ ) and polarization angle ( $\Delta \psi$ ) between the input signal map and the “observed” map in a  $10'$  diameter circular region centered on the galaxy, both with zero levels subtracted as described in Section 4.5. Both PPI1 and PPI4 are shown at native pixelization, yielding more than five times as many pixels in PPI1.

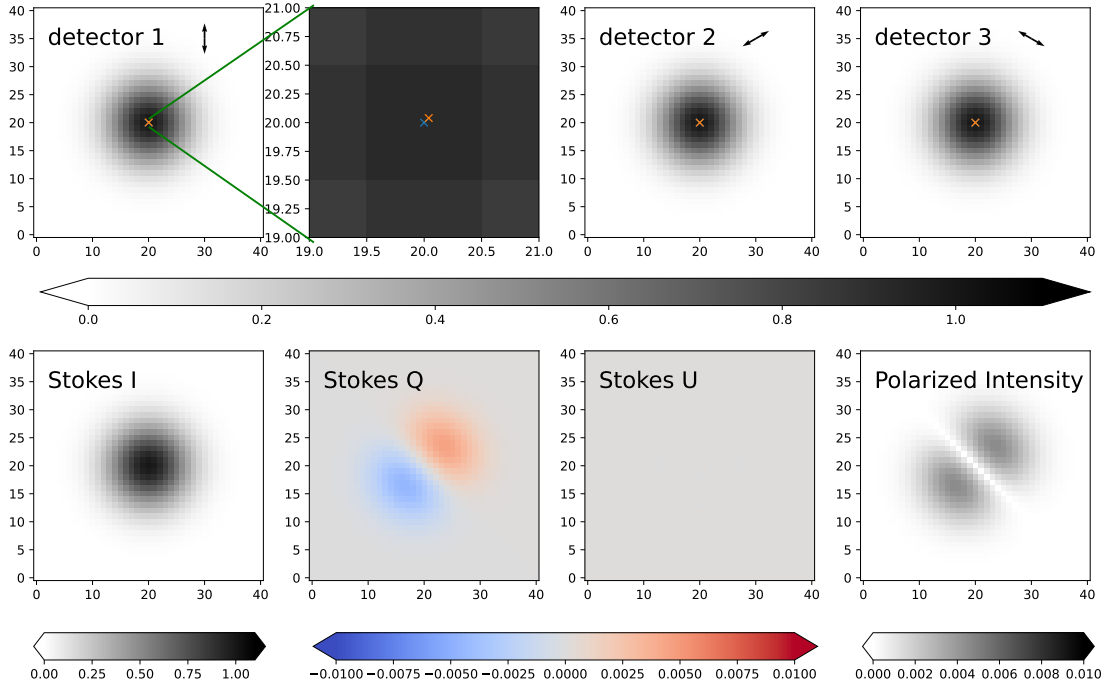


**Figure 10.** Demonstration of a polarization residual caused by relative pointing error. The top row shows the response of three detectors to an unpolarized, unresolved source. The three detectors have polarization response directions as shown by the vectors, and they are combined to solve for  $(I, Q, U)$ . The source as observed by detector 1 is displaced by 0.005 beam FWHM (as indicated by the red and blue X's in the inset) to simulate relative pointing knowledge error for that detector. The bottom row shows the resulting polarization artifacts, with a peak in polarized intensity of  $0.5\% \times$  the peak in total intensity.

Intensity gradients in the observed field enable relative alignment of the detectors sampling it. Order-of-magnitude, the uncertainty in the measured alignment shift ( $\Delta x, \Delta y$ ) of  $N$  detector samples is estimated by:

$$\sigma(\Delta x) \approx \frac{\sigma(I)}{\sqrt{N} \sqrt{\langle |\frac{dI}{dx}|^2 \rangle}}, \sigma(\Delta y) \approx \frac{\sigma(I)}{\sqrt{N} \sqrt{\langle |\frac{dI}{dy}|^2 \rangle}} \quad (19)$$

where  $\sigma(I)$  is the uncertainty in a single intensity measurement and  $\sqrt{\langle |\frac{dI}{dx}|^2 \rangle}$  is the root-mean-square intensity gradient in the  $x$  direction. For the central 6' diameter of NGC 6946, in the PPI4 band, the rms intensity gradient in one direction is  $\sim 2.5$  MJy/sr/arcsec. For the mean intensity of  $\sim 90$  MJy/sr in this region, the measurement uncertainty is  $\sim 1.9$  MJy/sr per detector per 350 Hz sample. If  $N \approx 30$  detectors overlapping the galaxy are used to measure the pointing, then the uncertainty in alignment (in 2D space) is  $\sim 0.2''$ , or  $0.007 \times$  the beam FWHM. This is near the pointing alignment target from earlier in this section, and the combination of multiple samples further improves the measurement.

A second effect is due to beam shape variation. Practicalities of optical design and instrument assembly mean there will be some variation in beam width and ellipticity across the field of view for a given PPI band. Another possible type of beam shape variation is beam ellipticity which aligns with the detector polarization direction. In either case, the detector differencing to derive polarization will show spatially-dependent residuals in  $Q$  or  $U$  resulting from differential response to  $I$ . This effect does not average down unless the scan pattern is changed in such a way that the patterns of residuals are changed in orientation or amplitude.

Differential width in the beam among the detectors measuring ( $I, Q, U$ ) creates an annular polarization residual around an unpolarized unresolved source, and  $\sim 1\%$  fractional difference in width causes a 0.5% peak in the polarized intensity. Differential ellipticity with direction uncorrelated with detector polarization orientation produces a quadrupolar residual in polarized intensity with similar sensitivity: a  $\sim 1\%$  fractional difference causes a 0.5% peak in the polarized intensity. Ellipticity aligning with the detector polarization produces more of an annular pattern.

Two mitigations for the beam shape effects are envisioned for PPI. One is implemented by the focal plane design, which has the three polarization angles well mixed and therefore guards against large-scale variations in beam shape across the focal plane. The other mitigation is implemented in the science data pipeline, if needed. A pipeline step smooths the measured data, using a convolution kernel customized to each detec-

tor, in order to better match the beam shapes in the maps. This smoothing occurs before the last solution for the ( $I, Q, U$ ) maps. It remains to be seen, from better knowledge of beam shapes and further simulation, whether the convolution step can be postponed until after the signal baselines (Section 3.4) are derived, or the convolution will need to be performed for each iteration.

A third potential beam effect is a different shape of the beam in the cross-polar direction. Ideally, there is no response for light polarized perpendicularly to the co-polar direction of the detector. However, for polarization efficiency  $\eta < 1$ , there is a weak response with likely a significantly different beam shape. For an unpolarized source, the cross-polar response produces only a slight modification of the beam shape — an asymmetry oriented with respect to the detector co- and cross-polar directions. The residuals in polarization are as described for differential beam width and ellipticity above. For a polarized source, the cross-polar response causes a polarization-dependent beam shape. This effect is expected to be negligible for achieving PRIMA's primary polarimetry science, but it will be studied in more detail in the future if needed.

## 7. CONCLUSIONS

In this paper, we have explored the performance of a novel concept for a polarimetric imager, that is proposed for the PRobe far-Infrared Mission for Astrophysics (PRIMA). Its particulars are that each focal plane is filled with single-polarization detectors equally sampling three linear polarization directions ( $120^\circ$  apart), and that it is not using a half-wave plate to modulate the incoming polarization. Using a realistic input sky, based on the driving polarization science case for PRIMA, and an observing strategy that makes use of the agile internal beam steering mirror, we demonstrate that even with pessimistic assumptions on the noise properties of the detectors, including its  $1/f$  component, a least-squares reconstruction approach provides an efficient way to recover polarimetric information on the source of interest to an accuracy level that satisfies the mission requirements.

More precisely, we find that reconstructed maps suffer only a 30-40% increase in noise level compared to the pure gaussian expectation. For a simulated 1.5 hour observation of the nearby galaxy NGC 6946, the polarized emission is detected with high signal-to-noise, both in the galaxy and cirrus foreground. In the region of interest in the simulation, the fidelity of the reconstructed information to the true information is excellent. Our simulations also show that PPI out-performs the sensitivity requirements set by the mission by a factor of

1.5-5 (depending on assumptions for the instrument and scan pattern), which are orders of magnitude better than what has been demonstrated to date.

While this will need to be demonstrated by relevant simulations, we expect to draw similar conclusions for a General Observer science case of PRIMA polarimetry, that of measuring magnetic fields and the nature of dust in degree-sized star-forming clouds (Moulet et al. 2023). Here as well, high-frequency modulation by the BSM, superimposed on slower spacecraft scanning motion, should allow the approach developed here to result in accurate and efficient map reconstruction.

#### ACKNOWLEDGMENTS

We acknowledge valuable feedback on the paper draft, simulator, and measurement approach provided

by Jochem Baselmans, Matt Bradford, David Chuss, Lorenza Ferrari, Laura Fissel, Jason Glenn, Willem Jellema, Margaret Meixner, and Stephen Yates.

This research was carried out in part at the Jet Propulsion Laboratory, California Institute of Technology, under a contract with the National Aeronautics and Space Administration.

*Facilities:* Herschel, VLA

*Software:* Astropy (Astropy Collaboration et al. 2013, 2018, 2022), Matplotlib (Hunter 2007), NumPy (van der Walt et al. 2011; Harris et al. 2020), SciPy (Virtanen et al. 2020)

#### REFERENCES

- Adami, O.-A., Rodriguez, L., Poglitsch, A., et al. 2019, *ApOpt*, 58, 398, doi: [10.1364/AO.58.000398](https://doi.org/10.1364/AO.58.000398)
- Andersson, B. G., Lazarian, A., & Vaillancourt, J. E. 2015, *ARA&A*, 53, 501, doi: [10.1146/annurev-astro-082214-122414](https://doi.org/10.1146/annurev-astro-082214-122414)
- Aniano, G., Draine, B. T., Hunt, L. K., et al. 2020, *ApJ*, 889, 150, doi: [10.3847/1538-4357/ab5fdb](https://doi.org/10.3847/1538-4357/ab5fdb)
- Arzoumanian, D., Furuya, R. S., Hasegawa, T., et al. 2021, *A&A*, 647, A78, doi: [10.1051/0004-6361/202038624](https://doi.org/10.1051/0004-6361/202038624)
- Astropy Collaboration, Robitaille, T. P., Tollerud, E. J., et al. 2013, *A&A*, 558, A33, doi: [10.1051/0004-6361/201322068](https://doi.org/10.1051/0004-6361/201322068)
- Astropy Collaboration, Price-Whelan, A. M., Sipőcz, B. M., et al. 2018, *AJ*, 156, 123, doi: [10.3847/1538-3881/aabc4f](https://doi.org/10.3847/1538-3881/aabc4f)
- Astropy Collaboration, Price-Whelan, A. M., Lim, P. L., et al. 2022, *ApJ*, 935, 167, doi: [10.3847/1538-4357/ac7c74](https://doi.org/10.3847/1538-4357/ac7c74)
- Barron, D., Ade, P., Anthony, A., et al. 2014, *Journal of Low Temperature Physics*, 176, 726, doi: [10.1007/s10909-013-1065-5](https://doi.org/10.1007/s10909-013-1065-5)
- Baselmans, J. J. A., Facchin, F., Pascual Laguna, A., et al. 2022, *A&A*, 665, A17, doi: [10.1051/0004-6361/202243840](https://doi.org/10.1051/0004-6361/202243840)
- Bendo, G. J., Griffin, M. J., Bock, J. J., et al. 2013, *MNRAS*, 433, 3062, doi: [10.1093/mnras/stt948](https://doi.org/10.1093/mnras/stt948)
- Béthermin, M., Bolatto, A. D., Boulanger, F., et al. 2024, *arXiv e-prints*, arXiv:2404.04320, doi: [10.48550/arXiv.2404.04320](https://doi.org/10.48550/arXiv.2404.04320)
- Borlaff, A. S., Lopez-Rodriguez, E., Beck, R., et al. 2023, *ApJ*, 952, 4, doi: [10.3847/1538-4357/acd934](https://doi.org/10.3847/1538-4357/acd934)
- Boselli, A., Eales, S., Cortese, L., et al. 2010, *PASP*, 122, 261, doi: [10.1086/651535](https://doi.org/10.1086/651535)
- Caldwell, R. R., Hirata, C., & Kamionkowski, M. 2017, *ApJ*, 839, 91, doi: [10.3847/1538-4357/aa679c](https://doi.org/10.3847/1538-4357/aa679c)
- Catalano, A., Ade, P., Atik, Y., et al. 2014, *A&A*, 569, A88, doi: [10.1051/0004-6361/201423868](https://doi.org/10.1051/0004-6361/201423868)
- Ching, T.-C., Qiu, K., Li, D., et al. 2022, *ApJ*, 941, 122, doi: [10.3847/1538-4357/ac9dfb](https://doi.org/10.3847/1538-4357/ac9dfb)
- Clark, S. E., Hill, J. C., Peek, J. E. G., Putman, M. E., & Babler, B. L. 2015, *PhRvL*, 115, 241302, doi: [10.1103/PhysRevLett.115.241302](https://doi.org/10.1103/PhysRevLett.115.241302)
- Draine, B. T., & Friaese, A. A. 2009, *ApJ*, 696, 1, doi: [10.1088/0004-637X/696/1/1](https://doi.org/10.1088/0004-637X/696/1/1)
- Draine, B. T., & Hensley, B. S. 2021, *ApJ*, 909, 94, doi: [10.3847/1538-4357/abd6c6](https://doi.org/10.3847/1538-4357/abd6c6)
- Dwek, E., Arendt, R. G., Fixsen, D. J., et al. 1997, *ApJ*, 475, 565, doi: [10.1086/303568](https://doi.org/10.1086/303568)
- Fissel, L. M. 2013, PhD thesis, University of Toronto, Canada
- Fissel, L. M., Ade, P. A. R., Angilè, F. E., et al. 2019, *ApJ*, 878, 110, doi: [10.3847/1538-4357/ab1eb0](https://doi.org/10.3847/1538-4357/ab1eb0)
- Friberg, P., Bastien, P., Berry, D., et al. 2016, in *Society of Photo-Optical Instrumentation Engineers (SPIE) Conference Series*, Vol. 9914, Millimeter, Submillimeter, and Far-Infrared Detectors and Instrumentation for Astronomy VIII, ed. W. S. Holland & J. Zmuidzinas, 991403, doi: [10.1117/12.2231943](https://doi.org/10.1117/12.2231943)
- Galitzki, N., Ade, P. A. R., Angilè, F. E., et al. 2014, in *Society of Photo-Optical Instrumentation Engineers (SPIE) Conference Series*, Vol. 9145, Ground-based and Airborne Telescopes V, ed. L. M. Stepp, R. Gilmozzi, & H. J. Hall, 91450R, doi: [10.1117/12.2054759](https://doi.org/10.1117/12.2054759)
- Geach, J. E., Lopez-Rodriguez, E., Doherty, M. J., et al. 2023, *Nature*, 621, 483, doi: [10.1038/s41586-023-06346-4](https://doi.org/10.1038/s41586-023-06346-4)
- Griffin, M. J., Abergel, A., Abreu, A., et al. 2010, *A&A*, 518, L3, doi: [10.1051/0004-6361/201014519](https://doi.org/10.1051/0004-6361/201014519)

- Guillet, V., Fanciullo, L., Verstraete, L., et al. 2018, *A&A*, 610, A16, doi: [10.1051/0004-6361/201630271](https://doi.org/10.1051/0004-6361/201630271)
- Harper, D. A., Runyan, M. C., Dowell, C. D., et al. 2018, *Journal of Astronomical Instrumentation*, 7, 1840008, doi: [10.1142/S2251171718400081](https://doi.org/10.1142/S2251171718400081)
- Harris, C. R., Millman, K. J., van der Walt, S. J., et al. 2020, *Nature*, 585, 357, doi: [10.1038/s41586-020-2649-2](https://doi.org/10.1038/s41586-020-2649-2)
- Hensley, B. S., & Draine, B. T. 2023, *ApJ*, 948, 55, doi: [10.3847/1538-4357/acc4c2](https://doi.org/10.3847/1538-4357/acc4c2)
- Hildebrand, R. H., Dotson, J. L., Dowell, C. D., Schleuning, D. A., & Vaillancourt, J. E. 1999, *ApJ*, 516, 834, doi: [10.1086/307142](https://doi.org/10.1086/307142)
- Hoang, T., Minh Phan, V. H., & Tram, L. N. 2023, *ApJ*, 954, 216, doi: [10.3847/1538-4357/ace788](https://doi.org/10.3847/1538-4357/ace788)
- Huffenberger, K. M., Rotti, A., & Collins, D. C. 2020, *ApJ*, 899, 31, doi: [10.3847/1538-4357/ab9df9](https://doi.org/10.3847/1538-4357/ab9df9)
- Hunter, J. D. 2007, *Computing in Science and Engineering*, 9, 90, doi: [10.1109/MCSE.2007.55](https://doi.org/10.1109/MCSE.2007.55)
- Johnson, B. R., Ade, P. A. R., Araujo, D., et al. 2014, *Journal of Low Temperature Physics*, 176, 741, doi: [10.1007/s10909-013-1014-3](https://doi.org/10.1007/s10909-013-1014-3)
- Jones, T. J., Klebe, D., & Dickey, J. M. 1992, *ApJ*, 389, 602, doi: [10.1086/171233](https://doi.org/10.1086/171233)
- Kane, E., Albert, C., Baselmans, J., et al. 2024, *Journal of Low Temperature Physics*, 214, 238, doi: [10.1007/s10909-023-03044-3](https://doi.org/10.1007/s10909-023-03044-3)
- Kennicutt, R. C., Calzetti, D., Aniano, G., et al. 2011, *PASP*, 123, 1347, doi: [10.1086/663818](https://doi.org/10.1086/663818)
- Krause, O., Lemke, D., Hofferbert, R., et al. 2006, in *Society of Photo-Optical Instrumentation Engineers (SPIE) Conference Series*, Vol. 6273, *Optomechanical Technologies for Astronomy*, ed. E. Atad-Ettedgui, J. Antebi, & D. Lemke, 627325, doi: [10.1117/12.671271](https://doi.org/10.1117/12.671271)
- Kurki-Suonio, H., Keihänen, E., Keskitalo, R., et al. 2009, *A&A*, 506, 1511, doi: [10.1051/0004-6361/200912361](https://doi.org/10.1051/0004-6361/200912361)
- Lamarre, J., Puget, J., Ade, P. A. R., et al. 2010, *A&A*, 520, A9, doi: [10.1051/0004-6361/200912975](https://doi.org/10.1051/0004-6361/200912975)
- Le Gouellec, V. J. M., Maury, A. J., & Hull, C. L. H. 2023, *A&A*, 671, A167, doi: [10.1051/0004-6361/202244865](https://doi.org/10.1051/0004-6361/202244865)
- Lopez-Rodriguez, E., Mao, S. A., Beck, R., et al. 2022, *ApJ*, 936, 92, doi: [10.3847/1538-4357/ac7f9d](https://doi.org/10.3847/1538-4357/ac7f9d)
- Mather, J. C. 1982, *ApOpt*, 21, 1125, doi: [10.1364/AO.21.001125](https://doi.org/10.1364/AO.21.001125)
- Meixner, M., Panuzzo, P., Roman-Duval, J., et al. 2013, *AJ*, 146, 62, doi: [10.1088/0004-6256/146/3/62](https://doi.org/10.1088/0004-6256/146/3/62)
- Meixner, M., Burgarella, D., Ciesla, L., et al. 2024, in *American Astronomical Society Meeting Abstracts*, Vol. 56, *American Astronomical Society Meeting Abstracts*, 457.13
- Moulet, A., Kataria, T., Lis, D., et al. 2023, *arXiv e-prints*, [arXiv:2310.20572](https://arxiv.org/abs/2310.20572), doi: [10.48550/arXiv.2310.20572](https://doi.org/10.48550/arXiv.2310.20572)
- Ngoc, N. B., Diep, P. N., Hoang, T., et al. 2023, *ApJ*, 953, 66, doi: [10.3847/1538-4357/acdb6e](https://doi.org/10.3847/1538-4357/acdb6e)
- Pattle, K., & Fissel, L. 2019, *Frontiers in Astronomy and Space Sciences*, 6, 15, doi: [10.3389/fspas.2019.00015](https://doi.org/10.3389/fspas.2019.00015)
- Pillai, T. G. S., Clemens, D. P., Reissl, S., et al. 2020, *Nature Astronomy*, 4, 1195, doi: [10.1038/s41550-020-1172-6](https://doi.org/10.1038/s41550-020-1172-6)
- Planck Collaboration XII. 2020, *A&A*, 641, A12, doi: [10.1051/0004-6361/201833885](https://doi.org/10.1051/0004-6361/201833885)
- Planck Collaboration Int. XIX. 2015, *A&A*, 576, A104, doi: [10.1051/0004-6361/201424082](https://doi.org/10.1051/0004-6361/201424082)
- Planck Collaboration Int. XXXIII. 2016, *A&A*, 586, A136, doi: [10.1051/0004-6361/201425305](https://doi.org/10.1051/0004-6361/201425305)
- Planck Collaboration Int. XXXV. 2016, *A&A*, 586, A138, doi: [10.1051/0004-6361/201525896](https://doi.org/10.1051/0004-6361/201525896)
- Planck Collaboration Int. XLII. 2016, *A&A*, 596, A103, doi: [10.1051/0004-6361/201528033](https://doi.org/10.1051/0004-6361/201528033)
- Poglitsch, A., Waelkens, C., Geis, N., et al. 2010, *A&A*, 518, L2, doi: [10.1051/0004-6361/201014535](https://doi.org/10.1051/0004-6361/201014535)
- Purcell, E. M. 1975, in *The Dusty Universe*, ed. G. B. Field & A. G. W. Cameron, 155–167
- Rieke, G. H. 1996, *Detection of Light: From the Ultraviolet to the Submillimeter* (Cambridge University Press)
- Ritacco, A., Ponthieu, N., Catalano, A., et al. 2017, *A&A*, 599, A34, doi: [10.1051/0004-6361/201629666](https://doi.org/10.1051/0004-6361/201629666)
- Soler, J. D., Alves, F., Boulanger, F., et al. 2016, *A&A*, 596, A93, doi: [10.1051/0004-6361/201628996](https://doi.org/10.1051/0004-6361/201628996)
- SPIRE. 2016, *SPIRE Data Reduction Guide*, SPIRE-RAL-DOC 003248. <https://www.cosmos.esa.int/documents/12133/1035800/SPIRE+Data+Reduction+Guide+For+HIPE+15>
- Stone, J. M., Marrone, D. P., Dowell, C. D., et al. 2016, *ApJ*, 825, 32, doi: [10.3847/0004-637X/825/1/32](https://doi.org/10.3847/0004-637X/825/1/32)
- Surgent, W. J., Lopez-Rodriguez, E., & Clark, S. E. 2023, *ApJ*, 954, 53, doi: [10.3847/1538-4357/ace4c0](https://doi.org/10.3847/1538-4357/ace4c0)
- Tauber, J. A., Mandolesi, N., Puget, J. L., et al. 2010, *A&A*, 520, A1, doi: [10.1051/0004-6361/200912983](https://doi.org/10.1051/0004-6361/200912983)
- Tram, L. N., Hoang, T., Lopez-Rodriguez, E., et al. 2021, *ApJ*, 923, 130, doi: [10.3847/1538-4357/ac13a1](https://doi.org/10.3847/1538-4357/ac13a1)
- van der Walt, S., Colbert, S. C., & Varoquaux, G. 2011, *Computing in Science and Engineering*, 13, 22, doi: [10.1109/MCSE.2011.37](https://doi.org/10.1109/MCSE.2011.37)
- Virtanen, P., Gommers, R., Oliphant, T. E., et al. 2020, *Nature Methods*, 17, 261, doi: [10.1038/s41592-019-0686-2](https://doi.org/10.1038/s41592-019-0686-2)
- Ward-Thompson, D., Karoly, J., Pattle, K., et al. 2023, *ApJ*, 946, 62, doi: [10.3847/1538-4357/acbea4](https://doi.org/10.3847/1538-4357/acbea4)
- Ysard, N., Jones, A. P., Guillet, V., et al. 2024, *A&A*, 684, A34, doi: [10.1051/0004-6361/202348391](https://doi.org/10.1051/0004-6361/202348391)